Observation of Rydberg exciton polaritons and their condensate in a perovskite cavity

Wei Bao[a,1], Xiaoze Liu[a,1], Fei Xue[b,c,d,1], Fan Zheng[e], Renjie Tao[a], Siqi Wang[a], Yang Xia[a], Mervin Zhao[a], Jeongmin Kim[a], Sui Yang[a], Quanwei Li[a], Ying Wang[a], Yuan Wang[a], Lin-Wang Wang[e], Allan H. MacDonald[b,2], and Xiang Zhang[a,f,2]

[a]NSF Nanoscale Science and Engineering Center, University of California, Berkeley, CA 94720; [b]Department of Physics, University of Texas at Austin, Austin, TX 78712; [c]Institute for Research in Electronics and Applied Physics, University of Maryland, College Park, MD 20742; [d]Maryland Nanocenter, University of Maryland, College Park, MD 20742; [e]Materials Sciences Division, Lawrence Berkeley National Laboratory, Berkeley, CA 94720; and [f]Faculties of Sciences and Engineering, University of Hong Kong, Hong Kong, China

Contributed by Allan H. MacDonald, August 22, 2019 (sent for review June 11, 2019; reviewed by Qing Gu and Chee Wei Wong)

The condensation of half-light half-matter exciton polaritons in semiconductor optical cavities is a striking example of macroscopic quantum coherence in a solid-state platform. Quantum coherence is possible only when there are strong interactions between the exciton polaritons provided by their excitonic constituents. Rydberg excitons with high principal value exhibit strong dipole–dipole interactions in cold atoms. However, polaritons with the excitonic constituent that is an excited state, namely Rydberg exciton polaritons (REPs), have not yet been experimentally observed. Here, we observe the formation of REPs in a single crystal $CsPbBr_3$ perovskite cavity without any external fields. These polaritons exhibit strong nonlinear behavior that leads to a coherent polariton condensate with a prominent blue shift. Furthermore, the REPs in $CsPbBr_3$ are highly anisotropic and have a large extinction ratio, arising from the perovskite's orthorhombic crystal structure. Our observation not only sheds light on the importance of many-body physics in coherent polariton systems involving higher-order excited states, but also paves the way for exploring these coherent interactions for solid-state quantum optical information processing.

Rydberg exciton | polariton | condensate | perovskite | cavity

Solid-state cavity quantum electrodynamics (CQED) delivers extraordinary control of light–matter interactions in various photonic structures (1). Beyond simply modifying the photonic density of states in the weak coupling regime, CQED also enables the formation of new hybrid light–matter quasiparticles called cavity polaritons (2, 3). In semiconductor microcavities, cavity polaritons are created by strong coupling between excitons and photons when the coupling rate is faster than the dissipation rates of both constituents. These bosonic quasiparticles possess a small effective mass ($\sim 10^{-4}$ electron mass)[2] from their photonic component and inherit strong interactions from their excitonic component. The combination leads to rich quantum optical phenomena, such as polariton condensation, superfluidity, and quantum vortices, that are similar to those seen in cold atom Bose–Einstein condensation, but at much elevated temperatures (4–8).

Polariton condensation relies on strong nonlinear polariton interactions via their matter constituent, and is characterized by a macroscopic coherent condensate of strongly interacting bosonic particles in a nonequilibrium state (4, 6, 9). The exciton–exciton interactions emerge from underlying Coulomb interactions and strongly depend on the dielectric environment and the exciton radius (4). Currently, the relatively delocalized Wannier–Mott excitons in inorganic semiconductors have formed polariton condensates at densities that are much lower than the exciton's Mott density (10–12), while the tightly bound Frenkel excitons in organic semiconductors have reached polariton condensation at high exciton densities around the exciton saturation density (13, 14). This difference is due to the larger exciton–exciton interaction strength for Wannier–Mott excitons (typical size, 3 to 10 nm) than for Frenkel excitons (typical size, <1 nm) (15), leading to orders of magnitude stronger interactions in Wannier–Mott excitons. Importantly, there are also excited states of Wannier–Mott excitons that are predicted to provide stronger dipole–dipole interaction strength in the framework of hydrogen-like Rydberg states (16). Polaritons with excitonic constituent of excited states, namely Rydberg exciton polaritons (REPs), have not been naturally observed, due to weak oscillator strength of the excitonic excited states in most optically active semiconductors.

Recently, the emerging lead halide perovskites with Rydberg exciton series (17, 18) have provided a high-quality optoelectronic platform that does not require sophisticated lattice-matched growth (19, 20). The group of lead halide perovskite semiconductors have bulk excitons with exceptional optical properties (21–25), such as a sizeable exciton binding energy, tunable band gaps, high quantum yield, and Rydberg exciton series of strong oscillator strength without applying external magnetic fields (17, 18, 26). They are therefore excellent candidates for investigating exciton–polariton states and polariton condensation, and even for future quantum photonic circuits (7). Encouragingly, polariton lasing based on the ground exciton state has recently been demonstrated in a $CsPbCl_3$ microcavity

Significance

Rydberg excitons with high principal value exhibit strong dipole–dipole interactions. However, polaritons with an excitonic constituent that is an excited state, namely Rydberg exciton polaritons (REPs), have not yet been experimentally observed. Here, we observe the formation of REPs in a single crystal $CsPbBr_3$ perovskite cavity without any external fields. These polaritons exhibit strong nonlinear behavior that leads to a coherent polariton condensate with a prominent blue shift. Furthermore, the REPs in $CsPbBr_3$ are highly anisotropic and have a large extinction ratio, arising from the perovskite's orthorhombic crystal structure.

Author contributions: W.B., X.L., and X.Z. conceived the idea and initiated the project; W.B. and X.L. conducted polariton experiments with assistance from R.T., S.W., Y.X., M.Z., J.K., S.Y., Q.L., Ying Wang, and Yuan Wang under the supervision of X.Z.; F.X. conducted polariton theoretical modeling under the supervision of A.H.M.; F.Z. and L.-W.W. preformed calculations of the band structure; W.B., X.L., F.X., A.H.M., and X.Z. analyzed data; and W.B., X.L., and X.Z. wrote the paper with assistance from all authors.

Reviewers: Q.G., University of Texas at Dallas; and C.W.W., University of California, Los Angeles.

The authors declare no conflict of interest.

[1]W.B., X.L., and F.X. contributed equally to this work.

[2]To whom correspondence may be addressed. Email: macdpc@physics.utexas.edu or xiang@berkeley.edu.

This article contains supporting information online at www.pnas.org/lookup/suppl/doi:10.1073/pnas.1909948116/-/DCSupplemental.

(27). In this work, we demonstrate the formation of hybrid exciton polaritons in single crystal perovskite $CsPbBr_3$, including emerging REPs without external fields. More importantly, we show that Bose–Einstein condensation of polaritons is reached with a prominent blue shift and interesting mode competition that can be explained by our quasiequilibrium mean-field theory. In addition, these polaritons are anisotropic with a large extinction ratio driven by the anisotropy of the potential landscape in the perovskite's orthorhombic phase (28). This precise polarization control is a necessary prerequisite in quantum optical information processing. This work represents a major step in solid-state quantum photonics systems, not only offering a unique platform for new quantum coherent many-body physics (29) but also opening a new door for solid-state quantum photonic applications in communication and computing (30).

The metal halide perovskite $CsPbBr_3$ is selected as the exciton host. Compared to hybrid organic–inorganic halide perovskites, all-inorganic $CsPbBr_3$ exhibits superior chemical stability and emission efficiency (31). Fig. 1*D* shows typical absorption spectra of a $CsPbBr_3$ crystal on mica at 100 K in its thermodynamically stable orthorhombic phase (see additional characterization in *SI Appendix*, *Materials and Methods* and Figs. S1–S3) (28) with clear absorption peaks (E_1 and E_2), consistent with the recent studies (18, 20). According to density functional theory (DFT) in the orthorhombic phase (Fig. 1*E*), there is only one exciton formed in the band edges of $CsPbBr_3$, where all other electronic are separated by more than 1 eV. The E_1 and E_2 peaks as the ground and first excited states (Rydberg series $n = 1, 2$) of the only exciton series are identified by the observed energy separation between the 2 absorption peaks, their temperature dependences (*SI Appendix*, Fig. S2), and the reported exciton binding energy (26). The orthorhombic phase also results in the mutually orthogonal birefringence along the ***a*** and ***b*** crystalline axes (Fig. 1 *C* and *E*).

To investigate the strong light–matter interactions in these excitonic states, we embedded the $CsPbBr_3$ microplate in a Fabry–Perot planar cavity (Fig. 1*A*), where the ***a*** and ***b*** axes are orthogonal along the in-plane surface. With the full cavity structure, the in-plane wavevector ***k*** of the cavity mode is also along this surface (Fig. 1 *A*, *Inset*). As shown in Fig. 1*B*, the microplate transferred onto a distributed Bragg reflector (DBR) substrate has a uniform thickness of 416 nm (*SI Appendix*, Fig. S1) and a typical square shape. Our cavity provides a quality factor in excess of a thousand, derived from the off-resonance cavity linewidth (*SI Appendix*, Fig. S6) as well as polariton linewidth from Fig. 2. This high cavity quality assists the formation of a REP, owing to the sharp interface between the perovskite and the metal mirror (*SI Appendix*, Fig. S1) as well as the reduced metal absorption losses at cryogenic temperature (32).

The coherent coupling of these states and cavity photons is revealed by *k*-space spectroscopy (*SI Appendix*, Fig. S12, for more details), when the sample is first cooled down to 90 K. The *k*-space characterization is carried out with selective linear polarization for both photoluminescence (PL) and reflectivity measurements (Fig. 2). The PL measurements are taken using a nonresonant pump laser of 460 nm diagonally polarized between

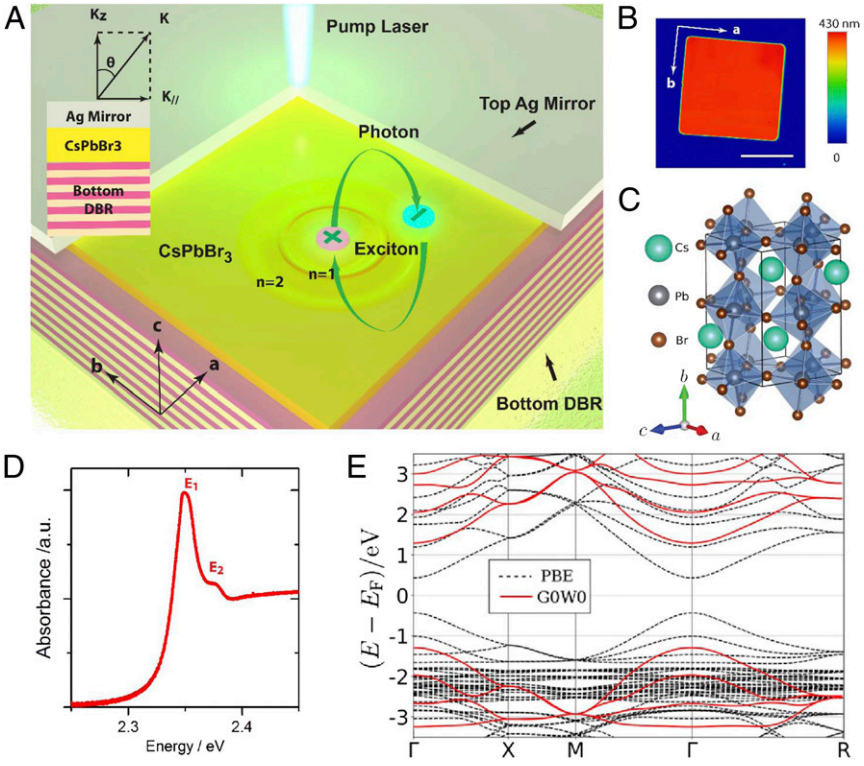

Fig. 1. Schematics of $CsPbBr_3$ microcavity devices and materials characterization. (*A*) The $CsPbBr_3$ microcavity is composed of a 16-pair SiO_2/Ta_2O_5 bottom distributed Bragg reflector (DBR), CVD-grown $CsPbBr_3$ microplates with a thickness of 416 nm, and a 55-nm-thick Ag top mirror. The crystal axes are also indicated. (*B*) Atomic force microscopy image of the uniform $CsPbBr_3$ square-shaped single-crystal perovskite used in combination with the bottom DBR mirror in the experiments summarized in Fig. 2. The crystal axes are also labeled. (Scale bar: 10 μm.) (*C*) The DFT calculated stable crystal structure of orthorhombic $CsPbBr_3$, with labeled ***a***, ***b***, and ***c*** crystalline axes. This structure results in almost identical refractive indices along the ***a*** and ***c*** axes, and a distinctly different refractive index along the ***b*** axis. (*D*) The polarization nonselective absorption spectrum of single-crystal $CsPbBr_3$ film on mica at 100 K. A prominent ground-state E_1 exciton absorption peak is clearly shown along with the excited $n = 2$ Rydberg exciton E_2 state. (*E*) Calculated PBE and G0W0 band structures for orthorhombic $CsPbBr_3$. With the inclusion of spin–orbit coupling, the PBE calculated band gap is corrected to 2.5 eV by G0W0, agreeing well with the experiments. Importantly, unlike GaAs, $CsPbBr_3$ has no degenerate or nearby band states at conduction or valance band edges (Γ point).

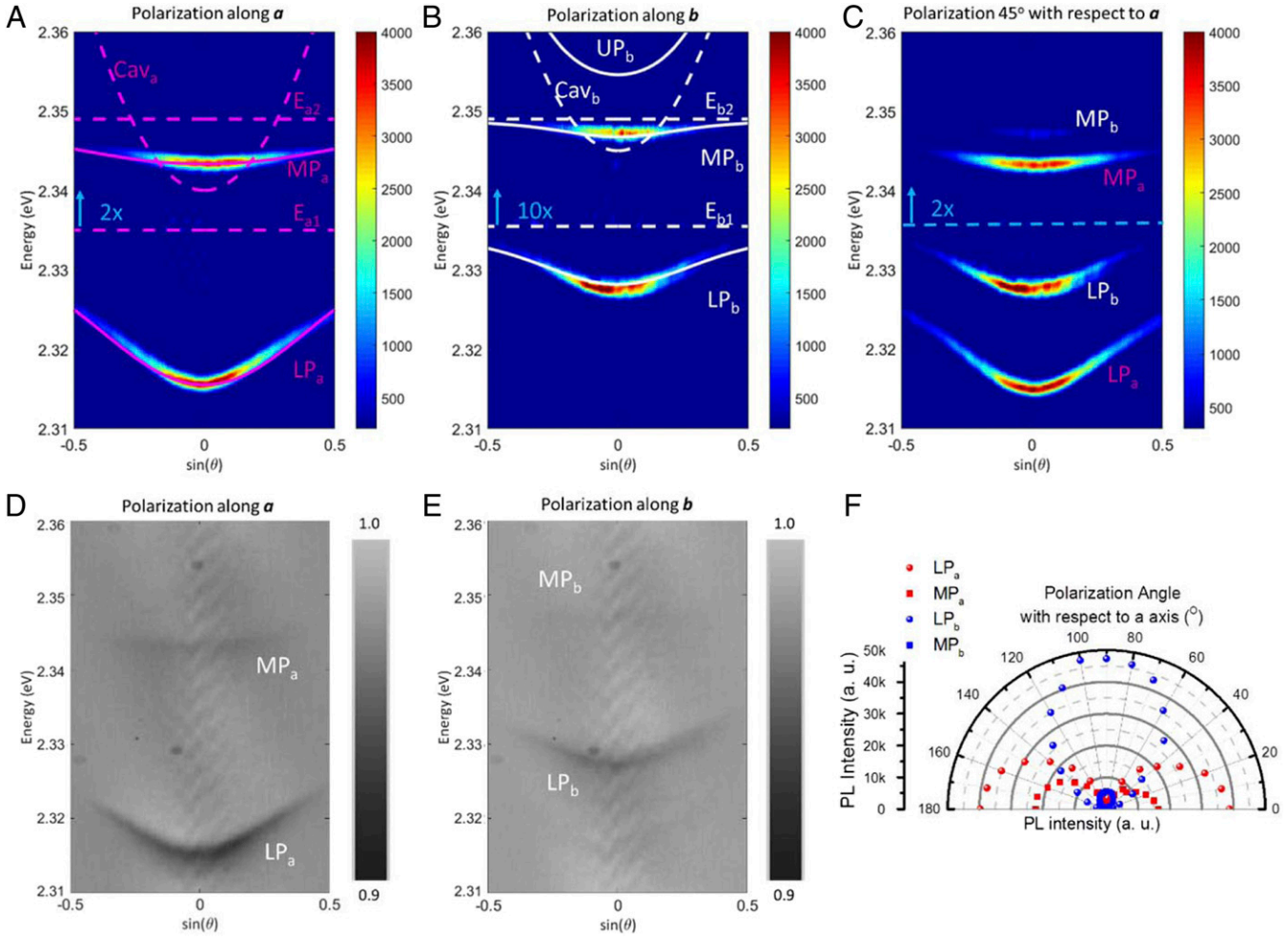

Fig. 2. The *k*-space angle-resolved PL and white light reflectivity at 90 K. The nonresonantly pumped (460-nm laser) PL map obtained by *k*-space spectroscopy with detection photon polarization (*A*) along crystal axis ***a***, (*B*) along crystal axis ***b***, and (*C*) 45° in between ***a*** and ***b*** axes (Fig. 1 *A* and *B*). The intensity of the middle branch polariton PL is magnified by 2×, 10×, and 2× in *A*–*C*, respectively, due to its weak emission. The horizontal axis represents the sine function of the emission light slant angles θ relative to the *z* axis (Fig. 1 *A*, *Inset*), and the vertical axis is the photon energy. Middle branch polariton MP_a and MP_b (better seen in *C*) are unambiguously formed due to the $n = 2$ exciton state. The polariton dispersion is fit using a coupled oscillator model. The exciton energy and photonic cavity mode (Cav_a and Cav_b) before strong coupling (dashed line) and the fitted polariton dispersion (solid line) are overlaid with the PL map. These fine excitonic states and their polariton structures can only be observed at low temperatures (<150 K). At higher temperatures, the cavity samples transit from only one lower polariton branch to a broad PL peak (similar to bare exciton emission). The corresponding polarization selective white light reflectivity maps of the same sample (*D*) along crystal axis ***a*** and (*E*) along crystal axis ***b***. The dispersion of *k*-space reflectivity maps matches the PL dispersion fit very well. (*F*) The polarization dependence of polariton emission at normal angle ($\theta = 0°$). The extinction ratio of these 2 orthogonal lower branch emission modes is more than 50.

a and ***b*** axes (at a 45°, as shown in Fig. 1*B*), while the reflectivity measurements are carried out using a nonpolarized tungsten halogen white light source. When the detection polarization is set along the ***a*** axis, 2 dispersive modes are observed from both PL (Fig. 2*A*) and reflectivity (Fig. 2*D*), identified as newly formed polariton states. Although *k*-space reflectivity has lower color contrast (low reflectivity dips of less than 10%) than PL, they have clear one-to-one correspondence for these polariton states. Both of these polariton modes are distinctively flattened at larger emission angles, indicating that the 2 excitonic states are strongly coupled with the cavity modes. By applying a coupled oscillator model with the 2 excitonic states and a cavity mode at slightly positive detuning ($\Delta_a = E_{cav} - E_{a1} = 5$ meV), the lower and middle branches (labeled as LP_a and MP_a, and overlaid with PL for better visibility) are consistent with the PL and reflectivity dispersion (Fig. 2 *A* and *D*; see the model fitting analysis in *SI Appendix*, Supplementary Note S1, additional supporting data in *SI Appendix*, Figs. S4 and S6, and the Hopfield coefficients in *SI Appendix*, Fig. S10). The upper branch (UP_a and UP_b) dominated by the photon mode component is not visible due to its weak oscillator strength and widely detuned cavity resonance, further aggravated in many cases by fast polariton relaxation (27). These 2 excitonic states corresponding to the $n = 1, 2$ states are confirmed to be in the strong coupling regime based on the temperature-dependent measurements (*SI Appendix*, Fig. S5). The 3-branch polariton dispersion holds up to 150 K, below which the $n = 1, 2$ states can be resolved with large binding energy and oscillator strengths. The polariton dispersion becomes 2-branch above 150 K, beyond which only the ground $n = 1$ state can be resolved. Based on the measurements of a variety of samples, the red shift of the exciton energy levels relative to Fig. 1 is due to sample-to-sample variations, PL Stokes shifts, and temperature-dependent band edge shift (see more details in *SI Appendix*, Figs. S2 and S3 and *Materials and Methods*), consistent with previous reports (13). Thus, this observation implies coherent strong coupling between light and an exciton excited state without an external field for the formation of REP. The extracted energy splittings (37.4 meV between LP_a

and MP_a, and 29.6 meV between MP_a and UP_a) are much larger than the polariton linewidth (~3 meV), demonstrating robust coherent coupling.

A similar PL dispersion has also been observed when setting the detection polarization along the ***b*** axis. By applying the same coupled oscillator model, the modes along the ***b*** axis are confirmed as strongly coupled REPs (labeled as LP_b and MP_b). Note that the polariton dispersion here is distinct from the ***a*** axis because of anisotropic refractive indices for the cavity modes, and different oscillator strengths along the 2 axes. When the detection polarization is along the ***a–b*** diagonal, the *k*-space PL map in Fig. 2*C* shows both sets of polariton dispersions linearly superimposed, suggesting that they are mutually orthogonal to each other. The independence of these polariton states is also seen in the PL intensities of each polariton branch (LP_a, MP_a, LP_b, and MP_b) in Fig. 2*F* with strong angular dependence (extinction ratio, >50) along the ***a*** and ***b*** axes, respectively. Thus, these polaritons show extremely strong polarization anisotropy originating from the perovskite refractive indices.

The polaritons can reach the nonlinear polariton condensation regime at large population densities of these polaritons. A polariton condensate is a coherent ensemble of a finite density of particles in the lowest available polariton state and can be described by a dissipative Bose–Einstein condensation model (4, 6, 7, 11, 33) (*SI Appendix*, Supplementary Note S3). A condensate is possible at elevated temperatures (cryogenic temperature and above), due to the small effective mass (~10^{-4} electron mass) of the hybrid light–matter particles and the strong interactions among them (4, 6, 7). The strong coupling regime of the REPs in Fig. 2 is observed in the linear regime with negligible interactions among them. At high carrier densities, the interactions become significant, generating a stimulated nonlinear regime, and eventually a macroscopically coherent quantum condensation state.

Polariton condensation can also be observed by performing *k*-space PL measurements at various pump powers. Here, we select a different sample with a more positive cavity detuning ($\Delta_a = E_{cav} - E_{a1} = 25.5$ meV), where the excitonic fraction is significantly larger to generate strong exciton interactions (4, 34) (see *SI Appendix*, Fig. S10, for the Hopfield coefficients). The 4 *k*-space PL map panels in Fig. 3*A*, labeled from *Left* to *Right* as $0.05P_{th}$, $0.4P_{th}$, P_{th}, and $1.4P_{th}$, clearly show nonlinear threshold behavior with increasing pump power. In Fig. 3, the threshold pump power P_{th} ~6.8 μJ/cm^2 pump pulse energy; the average P_{th} in various samples is around 2.4 μJ/cm^2 (see *SI Appendix*, Fig. S11, for another similar example and a statistical summary in *SI Appendix*, Supplementary Note S2). At each pump power, the detection polarization is set to be unpolarized so that both ***a*** and ***b*** polariton states can be observed. At pump power $0.05P_{th}$, the LP_a, MP_a, and LP_b modes are clearly detected and in excellent agreement with the coupled oscillator model (solid curves). As the pump power reaches $0.4P_{th}$, the lower LP_a and LP_b branches dominate the PL spectrum, with the PL intensity of LP_b increasing faster due to its higher excitonic fraction (see *SI Appendix*, Supplementary Note S3 and Fig. S10, for further discussion of exciton fractions). It is worth noting that the original parameters for the Rydberg levels in the coupled oscillator model have to be blue shifted for these REPs, indicating an energy modification caused by the excitonic interactions (35, 36). The effect is prominent until P_{th}. Importantly, the PL intensity of LP_a increases dramatically, compared with LP_b. When the pump power is increased slightly over P_{th} to 1.4 P_{th}, a full collapse of *k*-space PL dispersion into the bottom of LP_a, accompanied with a superlinear intensity increase and a large blue shift, which suggests that a condensate of these polaritons may have been reached. Moreover, the condensation process is also revealed by the lifetime data and statistics analysis (*SI Appendix*, Figs. S7 and S8).

We perform further analysis to confirm polariton condensation. In Fig. 3*B*, the PL intensity of LP_a along the normal emission angle and the corresponding linewidth versus pump power are plotted on log–log and linear–log scales. The "S"-shaped L–L curve of the PL intensity is divided into 3 regimes: the linear regime where polariton interactions are insignificant, a superlinear regime with a dramatic narrowing of linewidth due to the stimulated interactions between REPs, and the condensate regime in which most of REPs share the same lowest LP_a state (4). Note here that the average exciton density of perovskite devices at P_{th} is ~25 times lower than the exciton Mott density of the devices. This further justifies our interpretation of the nonequilibrium steady state as an exciton–polariton condensate rather than a normal photonic laser (see *SI Appendix*, Supplementary Note S2, for more details).

In contrast to conventional polariton condensation, where only one polariton mode responds to the nonlinear interaction process (4, 6, 7), here strong exciton–exciton interactions also lead to a unique condensation dynamics with multiple polariton modes involved. In Fig. 3*C*, the PL intensities of both LP_a and LP_b are plotted versus pump power. Below the threshold, the intensities of LP_a and LP_b increase with pump power independently. Due to the mutually orthogonal polarizations, these 2 modes barely cross talk in the linear regime. This can be confirmed by the intensity ratio between LP_a and LP_b below threshold shown in the solid black spheres of Fig. 3*C*. When the pump power exceeds threshold, the increasing density of LP_b does not contribute to the PL of LP_b, but directly interacts with other polaritons to establish the LP_a condensate. This dynamic process is elaborated in our theory analysis based on dissipative Gross–Pitaevskii equations (GPEs) in which LP_a is thermodynamically favored over LP_b when the stimulated scattering reaches a more stable final state (*SI Appendix*, Supplementary Note S3). The final condensation on the LP_a mode also suggests an efficient way to pin the polarization of the condensation, distinct from the stochastic polarization (37).

The strong interaction of the REPs in the nonlinear regime is also evident in the blue shifts of these polariton energies. This blue shift does not come from a heating effect at higher pump powers, as indicated by the similar shift under different pump conditions with significantly reduced heat (see control experimental data in *SI Appendix*, Fig. S9). The PL peak positions are extracted as a function of pump power for both LP_a and LP_b (Fig. 3*D*). Below the threshold, both polariton modes show noticeable blue shifts due to small disorder effect and the reservoir repulsive exciton–polariton contributions even when the densities are not large (35, 36, 38). Above the threshold, repulsive polariton–polariton interactions become more prominent causing the REP modes to show strong blue shifts. Although the potential renormalization will blue shift the condensation of LP_a as expected, the blue shift is quite significant while the LP_b intensity is saturated here. This suggests that polaritons of the LP_b modes actively contribute to the stimulated scattering process once the power is above the threshold (Fig. 3*C* and *SI Appendix*, Supplementary Note S3). We emphasize that the blue shift in both modes is almost 1/3 of the Rabi splitting, indicating very strong polariton interactions with the participation of Rydberg excitonic states. We have developed a theory model based on mean-field theory considering short-range exchange contributions and the dissipative GPEs to describe this large blue shift with ground state excitonic interactions (*SI Appendix*, Supplementary Notes S3 and S4, dot–dot–dash lines in Fig. 3*D*). Although exchange interaction between 2s excitons is surprisingly attractive rather than repulsive (details in *SI Appendix*, Supplementary Note S3), the 2s exciton fraction in the LP is significant smaller than 1s exciton, which makes this negative contribution negligible. It is worth noting that a detailed theory with quantitative analysis including dipole–dipole interactions (16) and interexciton interactions (1s–2s interactions) and accurate experimental calibration of polariton density to get the better

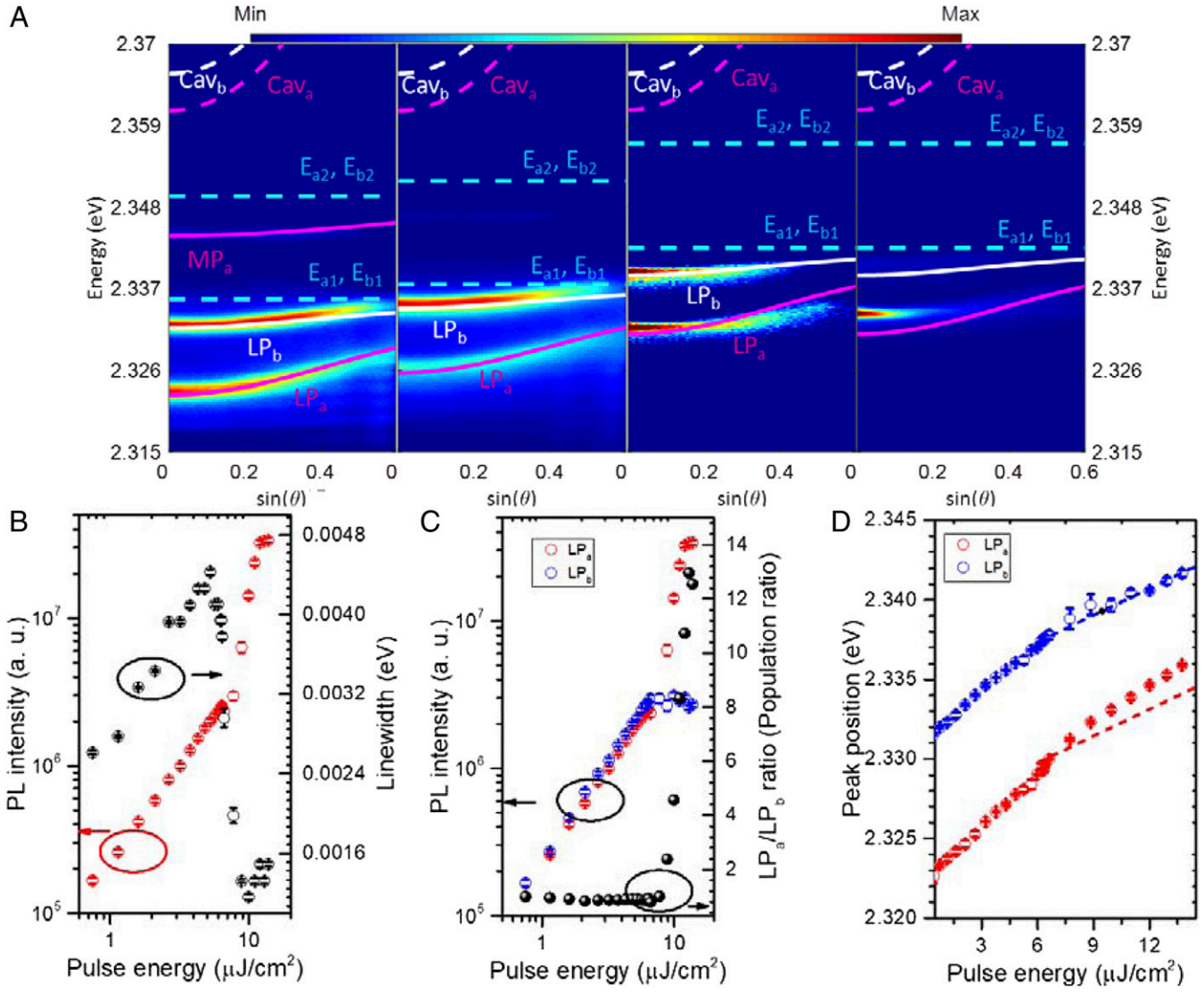

Fig. 3. Anomalous exciton–polariton condensate behavior at 55 K. (*A*) The *k*-space power-dependent angle resolved PL map taken at 0.05 P_{th}, 0.4P_{th}, P_{th}, and 1.4P_{th} (from *Left* to *Right*). The excitation is 460-nm light polarized along the ***a–b*** diagonal. The sample is slightly thinner and more positively detuned than in Fig. 2. The 2 sets of orthogonal Rydberg exciton–polariton modes are unambiguously identified and the polariton dispersions are fit using the same coupled oscillator model as in Fig. 2. The uncoupled exciton energy and photonic cavity mode dispersion (dashed line) and polariton dispersion fit (solid line) are overlaid with the PL map. The magenta color represents polarization mode along ***a*** axis, while the white color represents the orthogonal polarization mode along ***b*** axis (Fig. 1 *A* and *C*). The 1.4P_{th} panel shows the same fit as at P_{th} to emphasize the blue shift above the threshold. The small deviation in the high angle (sinθ) fitting of the polariton branch LP_a and LP_b at P_{th} and 1.4P_{th} is due to renormalization of the cavity mode at threshold. The polariton condensate experiences an anomalous condensation process in which the LP_b shows a faster increase than the lower-energy LP_a state between the second and third panels. This is due to a stronger exciton interaction along the ***b*** axis. As the pump density gets close to the condensation density, the LP_a finally experiences a superlinear increase with stimulated scattering to the lowest LP_a state, while LP_b shows no further increase. (*B*) Log–log plot of integrated PL intensity of LP_a mode at θ = 0° and full width at half-maximum (FWHM) of LP_a mode at θ = 0° versus pump power. Nonlinearity and linewidth narrowing of the polariton mode is observed as the excitation intensity exceeds the condensation threshold. Fitting error bars from the data processing are shown in *B–D*. (*C*) Log–log plot of both LP_a mode (red dot) and LP_b mode (blue dot) at θ = 0°. PL intensity and the ratio of the 2 modes versus pump power. (*D*) PL peak position of both LP_a mode (red dot) and LP_b mode (blue dot) at θ = 0° versus pump power. A strong blue shift of polariton modes below the threshold is observed due to the strong exciton interactions and potential system disorder (39). After the threshold of condensation, a prominent blue shift in both LP_a and LP_b mode results from the polariton–polariton interaction and the polariton–reservoir interaction. The theory predicted blue shift contributed from 1s–exciton-resulted polariton interaction is plot in red and blue dot–dot–dash line for guidance. The experimental observed value is larger than the estimation from pure 1s–exciton interaction.

estimate of interaction strength are beyond the scope of the current work. This experimental observation of REP with enhanced interactions promises future explorations of Rydberg interactions in solid-state systems.

In summary, we have surprisingly discovered REPs in a single crystal perovskite cavity, which enables coherent control of these fine quantum states. The intrinsic strong exciton interaction and optical birefringence in perovskite leads to the observation of polariton–condensation dynamics, which promises a robust macroscopically coherent state for quantum applications. This discovery presents a unique platform to study quantum coherent many-body physics, and potentially enables unprecedented manipulation of these Rydberg states by means such as chemical composition engineering, structural phase control, and external gauge fields.

Controlling the REP and its condensates not only adds flavors on studying polariton lasing, superfluidity, and vortices, but also holds great potential for important applications, such as communication, and quantum simulation.

Materials and Methods

Single-crystal $CsPbBr_3$ microplates are grown on 150-μm-thick high-quality muscovite mica substrates via chemical vapor deposition (CVD). The growth surfaces are placed face-down on the top of a quartz crucible that contained a fine power mixture with 20 mg of CsBr (Sigma-Aldrich; 99.999% purity) and 30 mg of $PbBr_2$ (Sigma-Aldrich; 99.999% purity). Tube pressure is maintained at ambient pressure with an Ar flow rate of 30 sccm. The system is first heated to 400 °C within 24 min, from 400 to 500 °C within 4 min and 30 sccm Ar, held at 500 °C for 20 min, and stopped afterward. When the temperature reaches ∼200 °C, the furnace is completely opened to achieve rapid cooling. The bottom 16 pairs of SiO_2 and Ta_2O_5 DBR are deposited on top via ion beam sputtering (Veeco IBS) to achieve ultrahigh flatness and >99.95% reflectivity. The as-grown $CsPbBr_3$ can be directly transferred from the mica substrate to the bottom DBR using a polydimethylsiloxane stamp, which is cured at room temperature and a mixture ratio of 7:1. Before e-beam evaporation of a top Ag mirror, we thermally evaporated 2-nm Al (3 samples, one in Fig. 2 and one in Fig. 3) or 10-nm Sb_2O_3 (one in *SI Appendix*, Fig. S6, and which can preserve PL quantum better) as a seeding layer followed by 5-nm Al_2O_3 atomic layer deposition (Oxford Instruments). Last, the sample is coated with 55-nm 99.99% purity silver using e-beam evaporation (CHA solution) with a pressure of $<5 \times 10^{-7}$ torr. The evaporation rate is set to be ∼1 nm/s to avoid oxidation during evaporation. All of the optical *k*-space measurements are carried out in a home-built confocal setup attached with a spectrometer and an electron-multiplying charge-coupled device camera (Andor spectrometer).

ACKNOWLEDGMENTS. W.B. thanks Prof. E. Yablonovitch for valuable advice and discussion of the manuscript. W.B., X.L., R.T., S.W., Y.X., M.Z., J.K., S.Y., Q.L., Ying Wang, Yuan Wang, and X.Z. acknowledge the support from the US Office of Naval Research Multidisciplinary University Research Initiatives (MURI) program (Grant N00014-17-1-2588) and the NSF under Major Research Instrumentation Grant 1725335. Work at University of Texas at Austin was supported by the Army Research Office Grant W911NF-17-1-0312 (MURI). F.X. acknowledges support under the Cooperative Research Agreement between the University of Maryland and the National Institute of Standards and Technology Physical Measurement Laboratory, Award 70NANB14H209, through the University of Maryland. F.Z. and L.-W.W. thank the Joint Center for Artificial Photosynthesis, a US Department of Energy Innovation Hub, supported through the Office of Science of the US Department of Energy under Award DE-SC0004993. F.Z. and L.-W.W. used the resources of National Energy Research Scientific Computing Center located in Lawrence Berkeley National Laboratory and the computational resources of the Oak Ridge Leadership Computing Facility at the Oak Ridge National Laboratory, under the Innovative and Novel Computational Impact on Theory and Experiment project. The authors also acknowledge the facility support at the Molecular Foundry by the US Department of Energy, Office of Science, Office of Basic Energy Sciences under Contract DE-AC02-05CH11231.

1. K. J. Vahala, Optical microcavities. *Nature* **424**, 839–846 (2003).
2. H. M. Gibbs, G. Khitrova, S. W. Koch, Exciton-polariton light-semiconductor coupling effects. *Nat. Photonics* **5**, 275–282 (2011).
3. C. Weisbuch, M. Nishioka, A. Ishikawa, Y. Arakawa, Observation of the coupled exciton-photon mode splitting in a semiconductor quantum microcavity. *Phys. Rev. Lett.* **69**, 3314–3317 (1992).
4. H. Deng, H. Haug, Y. Yamamoto, Exciton-polariton Bose-Einstein condensation. *Rev. Mod. Phys.* **82**, 1489–1537 (2010).
5. I. Carusotto, C. Ciuti, Quantum fluids of light. *Rev. Mod. Phys.* **85**, 299–366 (2013).
6. T. Byrnes, N. Y. Kim, Y. Yamamoto, Exciton-polariton condensates. *Nat. Phys.* **10**, 803–813 (2014).
7. D. Sanvitto, S. Kéna-Cohen, The road towards polaritonic devices. *Nat. Mater.* **15**, 1061–1073 (2016).
8. G. Khitrova, H. M. Gibbs, Nonlinear optics of normal-mode-coupling semiconductor microcavities. *Rev. Mod. Phys.* **71**, 1591–1639 (1999).
9. A. Imamoglu, R. J. Ram, S. Pau, Y. Yamamoto, Nonequilibrium condensates and lasers without inversion: Exciton-polariton lasers. *Phys. Rev. A* **53**, 4250–4253 (1996).
10. H. Deng, G. Weihs, C. Santori, J. Bloch, Y. Yamamoto, Condensation of semiconductor microcavity exciton polaritons. *Science* **298**, 199–202 (2002).
11. J. Kasprzak *et al*., Bose-Einstein condensation of exciton polaritons. *Nature* **443**, 409–414 (2006).
12. R. Balili, V. Hartwell, D. Snoke, L. Pfeiffer, K. West, Bose-Einstein condensation of microcavity polaritons in a trap. *Science* **316**, 1007–1010 (2007).
13. K. S. Daskalakis, S. A. Maier, R. Murray, S. Kéna-Cohen, Nonlinear interactions in an organic polariton condensate. *Nat. Mater.* **13**, 271–278 (2014).
14. J. D. Plumhof, T. Stöferle, L. Mai, U. Scherf, R. F. Mahrt, Room-temperature Bose-Einstein condensation of cavity exciton-polaritons in a polymer. *Nat. Mater.* **13**, 247–252 (2014).
15. V. M. Agranovich, Y. N. Gartstein, M. Litinskaya, Hybrid resonant organic-inorganic nanostructures for optoelectronic applications. *Chem. Rev.* **111**, 5179–5214 (2011).
16. V. Walther, R. Johne, T. Pohl, Giant optical nonlinearities from Rydberg excitons in semiconductor microcavities. *Nat. Commun.* **9**, 1309 (2018).
17. A. Miyata *et al*., Direct measurement of the exciton binding energy and effective masses for charge carriers in organic–inorganic tri-halide perovskites. *Nat. Phys.* **11**, 582–587 (2015).
18. Z. Yang *et al*., Unraveling the exciton binding energy and the dielectric constant in single-crystal methylammonium lead triiodide perovskite. *J. Phys. Chem. Lett.* **8**, 1851–1855 (2017).
19. Y. X. Chen *et al*., General space-confined on-substrate fabrication of thickness-adjustable hybrid perovskite single-crystalline thin films. *J. Am. Chem. Soc.* **138**, 16196–16199 (2016).
20. Q. Zhang *et al*., High-quality whispering-gallery-mode lasing from cesium lead halide perovskite nanoplatelets. *Adv. Funct. Mater.* **26**, 6238–6245 (2016).
21. L. M. Pazos-Outón *et al*., Photon recycling in lead iodide perovskite solar cells. *Science* **351**, 1430–1433 (2016).
22. M. M. Lee, J. Teuscher, T. Miyasaka, T. N. Murakami, H. J. Snaith, Efficient hybrid solar cells based on meso-superstructured organometal halide perovskites. *Science* **338**, 643–647 (2012).
23. B. R. Sutherland, E. H. Sargent, Perovskite photonic sources. *Nat. Photonics* **10**, 295–302 (2016).
24. J.-C. Blancon *et al*., Extremely efficient internal exciton dissociation through edge states in layered 2D perovskites. *Science* **355**, 1288–1292 (2017).
25. S. D. Stranks, H. J. Snaith, Metal-halide perovskites for photovoltaic and light-emitting devices. *Nat. Nanotechnol.* **10**, 391–402 (2015).
26. K. Galkowski *et al*., Determination of the exciton binding energy and effective masses for methylammonium and formamidinium lead tri-halide perovskite semiconductors. *Energy Environ. Sci.* **9**, 962–970 (2016).
27. R. Su *et al*., Room-temperature polariton lasing in all-inorganic perovskite nanoplatelets. *Nano Lett.* **17**, 3982–3988 (2017).
28. D. Zhang, S. W. Eaton, Y. Yu, L. Dou, P. Yang, Solution-phase synthesis of cesium lead halide perovskite nanowires. *J. Am. Chem. Soc.* **137**, 9230–9233 (2015).
29. M. Saffman, T. G. Walker, K. Mølmer, Quantum information with Rydberg atoms. *Rev. Mod. Phys.* **82**, 2313–2363 (2010).
30. H. J. Kimble, The quantum internet. *Nature* **453**, 1023–1030 (2008).
31. L. Protesescu *et al*., Nanocrystals of cesium lead halide perovskites ($CsPbX_3$, X = Cl, Br, and I): Novel optoelectronic materials showing bright emission with wide color gamut. *Nano Lett.* **15**, 3692–3696 (2015).
32. S. V. Jayanti *et al*., Low-temperature enhancement of plasmonic performance in silver films. *Opt. Mater. Express* **5**, 1147 (2015).
33. C. Schneider *et al*., An electrically pumped polariton laser. *Nature* **497**, 348–352 (2013).
34. O. Jamadi *et al*., Polariton condensation phase diagram in wide-band-gap planar microcavities: GaN versus ZnO. *Phys. Rev. B* **93**, 115205 (2016).
35. M. D. Lukin *et al*., Dipole blockade and quantum information processing in mesoscopic atomic ensembles. *Phys. Rev. Lett.* **87**, 037901 (2001).
36. P. Grünwald *et al*., Signatures of quantum coherences in Rydberg excitons. *Phys. Rev. Lett.* **117**, 133003 (2016).
37. J. J. Baumberg *et al*., Spontaneous polarization buildup in a room-temperature polariton laser. *Phys. Rev. Lett.* **101**, 136409 (2008).
38. T. Kazimierczuk, D. Fröhlich, S. Scheel, H. Stolz, M. Bayer, Giant Rydberg excitons in the copper oxide Cu_2O. *Nature* **514**, 343–347 (2014).
39. Y. Sun *et al*., Direct measurement of polariton-polariton interaction strength. *Nat. Phys.* **13**, 870–875 (2017).